RSC Advances

PAPER

View Article Online
View Journal | View Issue

Cite this: *RSC Adv.*, 2021, **11**, 32955

Study on the performance of a MOF-808-based photocatalyst prepared by a microwave-assisted method for the degradation of antibiotics

Fangwai Wang,[ab] Ruixue Xue,[ab] Yujie Ma,[ab] Yizhao Ge,[ab] Zijun Wang,[*ab] Xiuwen Qiao*[a] and Paiang Zhou[a]

In this paper, a simple method was used to rapidly prepare MOF-808 with a large specific surface area and high stability. Bi_2S_3 and MOF-808 were used to design and synthesize high-stability Bi_2S_3/MOF-808 nanocomposites, which were then used for the photocatalytic degradation of antibiotic tetracyclines. The performance test results showed that the 0.7-808 composite material had good photocatalytic degradation performance for tetracycline under visible-light irradiation, and the degradation rate reached 80.8%, which was 3.21 times and 1.76 times that of MOF-808 and Bi_2S_3, respectively. This was mainly due to the high photocurrent response and photoluminescence of the Bi_2S_3/MOF-808 composite material. Therefore, the close contact of n–n Bi_2S_3/MOF-808 can transfer light-generated electrons and holes to improve the utilization efficiency of photogenerated charges, thereby greatly improving the photocatalytic reaction activity. Particle-capture experiments and ESR confirmed that $^{\bullet}OH$ was the main active substance in the photocatalytic degradation.

Received 30th June 2021
Accepted 26th August 2021

DOI: 10.1039/d1ra05058c

rsc.li/rsc-advances

1. Introduction

In recent years, with the development and demands of modern industrialization, antibiotics have been widely used in medical care and animal husbandry. However, the excessive use of antibiotics has caused serious water pollution.[1–3] Facing the progressively serious water pollution and energy crisis, there is an urgent need to develop an efficient and green technology to solve these problems. Due to its environmental friendliness, low energy consumption and low cost, the photocatalysis of semiconductor materials is considered to be an effective candidate method to solve antibiotic pollution in water, and this technology has received more and more attention.[4,5] However, compared with dyes and other pollutants, the photocatalytic degradation of antibiotics is relatively difficult.[6,7] Therefore, it is necessary to develop new effective photocatalysts with higher antibiotic degradation efficiency. In addition, the photogenerated carriers of the catalyst have strong oxidizing and reducing properties, and can quickly degrade pollutants, which has become one of the effective ways to remove water pollution.[8–10] Nowadays, researchers have devoted themselves to the study of high-efficiency semiconductor photocatalysts.

Metal–organic frameworks (MOFs) are a new type of crystalline porous materials with a periodic network framework structure formed by the self-assembly of organic ligands and inorganic metal centers (metal ions or metal clusters). The materials have the advantages of a large specific surface area, high porosity, and a designable structure.[11–14]

As a new type of photocatalyst, MOFs have the following advantages: (1) high porosity: there are more channels for the transport of substrates and products and more exposed reactive sites, which is conducive to the rapid transfer and utilization of photogenerated charges, and reduces the recombination rate of electrons–holes in the photocatalytic system. (2) Adjustable porous structure: the introduction of groups with a long-spectral effect, such as organic ligands, can broaden the light-response range of MOFs, and allow realizing the visible-light and even near-infrared photocatalysis of MOFs, so that they can generate more electron–hole pairs under sunlight irradiation.[15] (3)There are structural defects: these are usually recombination centers for photogenerated electron–hole pairs in the catalyst, which together with MOFs having an ordered crystalline structure is beneficial for inhibiting the recombination of photogenerated electrons and holes. (4) Similar semiconductor features are easy to recombine with some nanomaterials to form heterojunctions or Schottky structures.[16]

MOF-808 is a polyhedral structure formed with metal zirconium (Zr) as a unit. In addition, Zr-based MOF has good stability. The polyhedral framework structure gives it a large specific surface area.[17] A variety of semiconductor materials can use it as a carrier or form a heterojunction to improve the photocatalytic activity. However, due to its wide band gap (4.03

[a]*School of Chemistry and Chemical Engineering, Key Laboratory for Green Processing of Chemical Engineering of Xinjiang Bingtuan, Shihezi University, Beisi Road, Shihezi, Xinjiang 832003, P. R. China. E-mail: wzj_tea@shzu.edu.cn; Tel: +86 15699322089*
[b]*Carbon Neutralization and Environmental Catalytic Technology Laboratory, Shihezi University, Shihezi 832003, P. R. China*

eV), MOF-808 can only absorb less than 321 nm ultraviolet light, and the visible-light-utilization rate is extremely low, which greatly limits the wide application of MOF-808 in the photocatalytic treatment of water pollution. Therefore, it is particularly important to find a semiconductor material to modify MOF-808 to broaden its light-response range.

Bismuth sulfide (Bi_2S_3) has attracted extensive attention from researchers as a narrow band gap (1.3–1.7 eV) semiconductor photocatalyst with an extremely high utilization of visible light.[18] It can be easily excited to generate electron–hole pairs under visible light, and Bi_2S_3 is non-toxic, so it is considered to be a promising semiconductor material. As a semiconductor photocatalyst, Bi_2S_3 has a cut-off absorption wavelength of about 930 nm, and has a strong absorption capacity in the full visible-light region and even in part of the infrared light region.[19] However, the band gap of pure Bi_2S_3 is relatively narrow, so it can easily aggregate. The photogenerated electron–hole pairs under visible-light irradiation can easily recombine, which greatly reduces the number of electrons as the main active species, resulting in a low concentration of active species, so the photocatalytic performance is poor. In general, it is difficult to improve the activity of single-component photocatalytic semiconductor materials. Therefore, the introduction of a new energy band into band gap and other energy band engineering is a basic strategy to improve the photocatalytic activity.[20]

In this paper, MOF-808 with a large specific surface area and high stability was prepared simply and quickly by using a microwave oven. According to the previously reported literature,[21,22] the Bi_2S_3/MOF-808 composite was then prepared by a hydrothermal method and applied to the photocatalytic degradation of tetracycline. The 0.7-808 composite catalyst had the best catalytic degradation performance. Under visible light, the degradation rate of tetracycline reached 80.8%, which was 3.21 times and 1.76 times that of simple MOF-808 and bismuth sulfide, respectively. This was mainly due to the high photocurrent response and photoluminescence of the Bi_2S_3/MOF-808 composite material. Bi_2S_3 tightly connects with MOF-808 after contacting, which can transfer electrons and holes generated by light, improve the utilization efficiency of photogenerated charges, and greatly improve the photocatalytic reaction activity. Particle-capture experiments and ESR confirmed that $^{\cdot}OH$ was the main active substance in the photocatalytic degradation.

2. Experimental

2.1 Materials

The L-cysteine, absolute ethanol, tetracycline, 1,3,5-benzenetricarboxylic acid, zirconium oxychloride octahydrate, bismuth nitrate pentahydrate, and other chemicals used in the experiment were all analytically pure (99%) without further purification. Deionized water was used in all the experimental work in this study. All the medicines come from Titan.

2.2 Sample preparation

2.2.1 Preparation of the MOF-808. A mixture of H_3BTC (0.210 g) and $ZrOCl_2 \cdot 8H_2O$ (0.967 g) was dissolved in the mixed solvent DMF/formic acid (1 : 1) in a 200 mL reaction flask. Then the mixture was put into a microwave oven and heated over a medium heat for about 5 min. After centrifugation, filtration, and washing with DMF, then shaking for 10–15 min, this operation was repeated three times, before finally putting the mixture into the vacuum oven and drying it at 60 °C for about 12 h. After drying, a white powder was obtained.

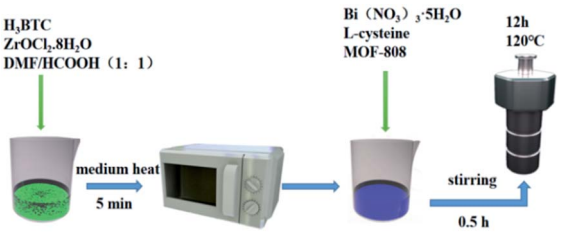

Fig. 1 Schematic illustration of the preparation of the Bi_2S_3/MOF-808 composite.

2.2.2 Preparation of Bi_2S_3/MOF-808. First, 1.94 g of $Bi(NO_3)_3 \cdot 5H_2O$ was accurately weighed in a 250 mL beaker and 20 mL of deionized water added, with stirring for 10 min to dissolve the material. Then, 0.728 g of L-cysteine was accurately weighed in a 100 mL beaker, and 40 mL of deionized water was added to dissolve it, and then a certain proportion of MOF-808 (for the different contents of MOF-808 of 10%, 30%, 50%, 70% and 90% (mass percentage), respectively) was added. The obtained samples are expressed as 0.1-808, 0.3-808, 0.5-808, 0.7-808, 0.9-808, respectively. After 20 min of ultrasound, the mixed solution was slowly added into the previous $Bi(NO_3)_3 \cdot 5H_2O$ solution and stirred for 30 min. The stirred solution was transferred to a 100 mL stainless steel reactor, heated at 120 °C for 12 h, and then washed three times with anhydrous ethanol and deionized water, centrifuged and filtered, and dried at 60 °C in the vacuum oven.

The preparation of pure Bi_2S_3 is the same as above, except that MOF-808 is not added. A schematic illustration of the preparation of Bi_2S_3/MOF-808 composite can be seen in Fig. 1.

2.3 Characterization of the photocatalysts

D8 ADVANCED powder X-ray diffraction (XRD, Cu-Kα radiation, $\lambda = 1.5418$ Å) and Nexus 470 Fourier-transform infrared spectrometry were used to test the phase structure of the samples. A Nicolet iS10 Fourier-transform infrared (FTIR) spectrometer was employed to record the FTIR spectra of the samples in the wavenumber range of 500–4000 cm^{-1}. A JSM-7001F field emission scanning electron microscopy (SEM) system and JEM-2100 transmission electron microscopy (TEM) system were used to characterize the morphology and microstructure of the sample. The ESCAPHI 500 X-ray photoelectron spectroscopy (XPS) system was used to determine the element composition and valence state distribution of the surface. A UV-2450 UV-vis spectrophotometer (UV-vis DRS) with barium sulfate as the substrate was used to test the light-absorption performance of the sample. A Cary Eclipse fluorescence spectrometer was used to measure the photoluminescence (PL) performance of the

sample. A CHI660D electrochemical workstation was used to test the photocurrent, impedance, and Mott–Schottky plots were performed for the samples. The low-temperature electron spin resonance (ESR spectrum) of the prepared sample was measured using a Bruker EXMEPR spectrometer at liquid nitrogen temperature (77 K).

2.4 Photocatalytic activity

The photocatalytic activity of all the samples was tested by simulating organic pollutants with tetracycline (CP) aqueous solution under simulated visible-light irradiation. The specific steps were as follows: the photoreaction experiments of different organic pollutants were similar, that is, 50 mg sample and 50 mL corresponding pollutant solution (CP, 20 mg L^{-1}) were added into the photocatalytic reactor, and the reactor was placed in the photocatalytic reactor (equipped with a 300 W xenon lamp and a filter (≥420 nm) (CEL-HXF300, Beijing, China)), and the stirring was turned on to mix the catalyst and solution evenly. The catalyst was stirred in the dark for 30 min to achieve adsorption–desorption equilibrium between the organic pollutants and catalyst. After turning on the lamp, the water circulation system was opened to maintain the reaction system at 25 °C to eliminate the deviations of light temperature. Within a certain interval, 6 mL of the suspension was taken with a syringe and centrifuged at 9000 rpm for 15 min, and an ultraviolet visible spectrophotometer (UV-31/32/3300) was used to analyze and determine the characteristic absorption peak of CP at 358 nm, so as to determine the degree of photocatalytic degradation. In order to ensure the repeatability of the results, three parallel experiments were conducted to obtain the average value of each group of conditions. A blank test was also performed by irradiating the reactant solution in the absence of a catalyst to evaluate its light-induced self-sensitive photodegradation.

$$\eta = \frac{C_0 - C_t}{C_0} \times 100\%$$

In the formula, η is the photocatalytic efficiency; C_0 is the concentration of the reactants before illumination, and C_t is the concentration of the reactant after t hours of illumination.

3. Results and discussion

3.1 Structural and textural properties of Bi_2S_3/MOF-808

3.1.1 XRD and FTIR analysis. The crystallinity of Bi_2S_3, MOF-808, and of the Bi_2S_3/MOF-808 nanocomposites was investigated by XRD, as seen in Fig. 2(a). The XRD patterns of the composites with different Bi_2S_3 loadings showed that strong diffraction peaks appeared at 2θ of 8.36° and 8.74°, corresponding to the (311) and (222) crystal planes. The two diffraction peaks were the MOF-808 characteristic peak, and this result was consistent with the diffraction peak of MOF-808 reported in the literature,[23] indicating that MOF-808 was successfully prepared, as well indicating that the crystallinity of MOF-808 increased with the increase in Bi_2S_3 loading decline

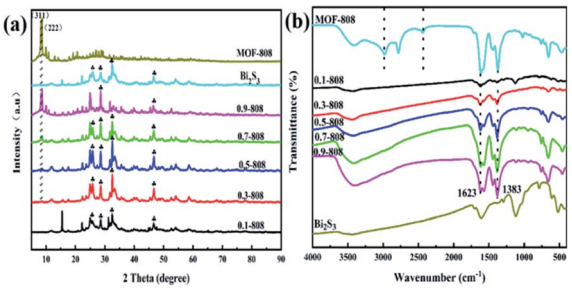

Fig. 2 (a) Typical XRD patterns and (b) the FTIR spectra of MOF-808, Bi_2S_3 and 0.7-808.

and then disappeared. In addition, the XRD pattern diffraction peaks of each sample were consistent with the orthorhombic Bi_2S_3 standard card (JCPDS no. 17-0320), and 2θ = 24.93°, 28.61°, 31.80°, 46.66°, respectively. There were four strong diffraction peaks and these were very sharp, corresponding to the crystal planes (130), (211), (221), (501), respectively. This confirmed that the prepared sample was Bi_2S_3. However, the diffraction peaks of Bi_2S_3 and its complexes had miscellaneous peaks. Therefore, it was inferred that this was not Bi_2S_3, but rather may be the L-cysteine. After adding L-cysteine, because L-cysteine contains –SH, $–NH_2$, and –COOH functional groups, it can form a complex with Bi^{3+} when reacting. When the temperature rises, Bi_2S_3 crystal nuclei quickly form in the reaction system.[24,25] It can be seen from the infrared spectrum Fig. 2(b) that the characteristic peak of 1623 cm^{-1} could be attributed to the asymmetric stretching vibration of –COO connected to the deprotonated –COOH and metal Zr, and the characteristic peak of 1383 cm^{-1} could be attributed to the symmetric stretching vibration of the upper COOH. These two characteristic peaks are the characteristic peak of MOF-808.[26] It is worth noting that the characteristic peaks of MOF-808 could be seen in all the complexes, which once again showed that Bi_2S_3/MOF-808 was successfully prepared. However, some peaks appeared between 3000 and 2500 cm^{-1}, and it is speculated that there may have been some unreacted pyromellitic acid or crystal water.

3.1.2 SEM/TEM and EDS analyses. The morphology and structure of the monomer and the composite materials were characterized by SEM and TEM, and the results are as follows. The SEM image of pure MOF-808 is shown in Fig. 3(a) it can be seen that the MOF-808 synthesized by microwave had relatively regular crystal grains with a particle size of about 500 nm and was accompanied by many pore-like structures. At the same time, the SEM image of Bi_2S_3 in Fig. 3(b) shows that the length was between 500 nm and 1 μm in the rod-like structure, but most of the rod-like structures were in a stacked state. The SEM of 0.7-808 showed that Bi_2S_3 was dispersed on MOF-808, and the structural state can also be seen from Fig. 3(c), where it can be clearly observed that the two materials were closely combined together.

Compared with pure Bi_2S_3, Bi_2S_3 was more dispersed in the 0.7-808 composite material, which could increase the photoreaction area during the photocatalytic reaction process and

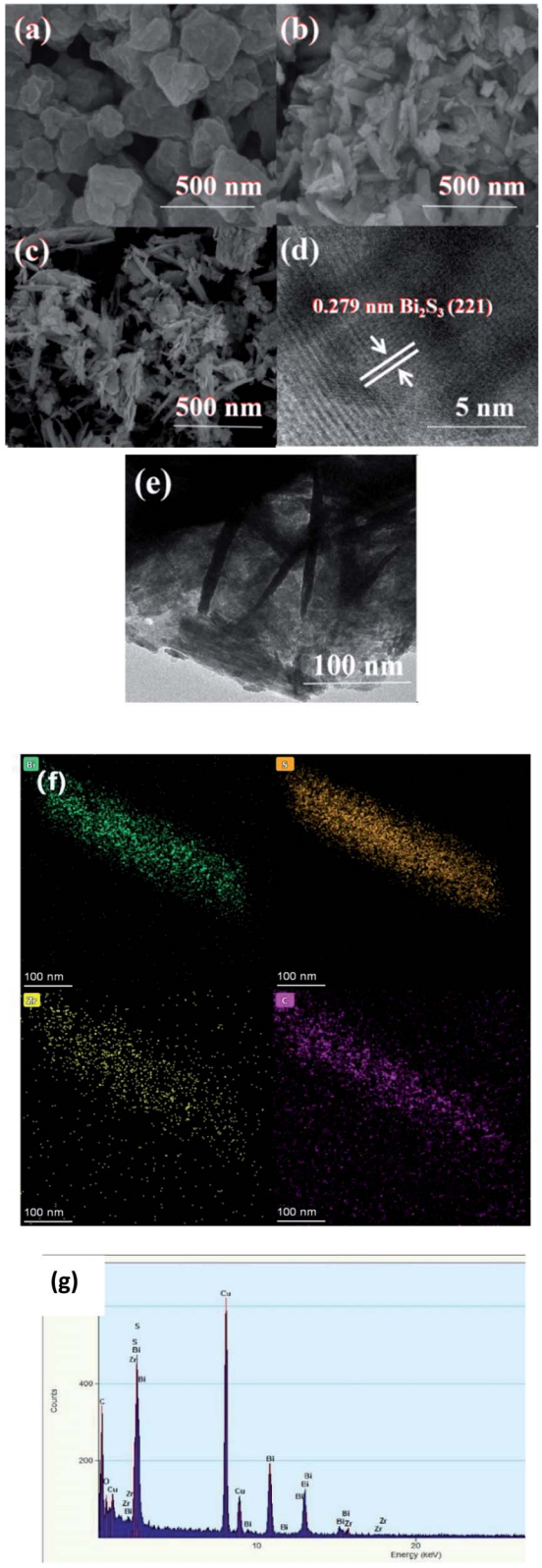

Fig. 3 SEM images of (a) MOF-808; (b) Bi_2S_3; (c) 0.7-808, (d) HRTEM images of 0.7-808, (e) TEM images of 0.7-808, (f) elemental mappings of 0.7-808, (g) EDS spectrum of 0.7-808.

further improve the photocatalytic activity. In order to analyze its structure more deeply, 0.7-808 was characterized by TEM and high-resolution TEM (HRTEM). Fig. 3(d) presents the HRTEM images of 0.7-808, in which a lattice fringe with a width of 0.279 nm can be clearly seen, which corresponds to the (221) crystal plane of Bi_2S_3. The result is consistent with those of XRD. In addition, the EDS spectrum images and elemental mappings were used to reveal the microstructure and composition of 0.7-808. As shown in Fig. 3(f) and (g), it is obvious that the 0.7-808 composite material was composed of C, O, Zr, S, and Bi elements, which fully proves the successful synthesis of the 0.7-808 composite material.

3.1.3 XPS analysis. The surface chemical composition of Bi_2S_3/MOF-808 was analyzed by XPS and the results are shown in Fig. 4 the XPS survey spectrum (Fig. 4(a)) showed that the pure Bi_2S_3 contained Bi and S elements, the pure MOF-808 contained C, O, and Zr elements, and the composite contained Bi, S, C, O, and Zr 5 elements, which were consistent with the XRD results. The narrow-scan spectra of Zr $3d_{3/2}$ and Zr $3d_{5/2}$ showed binding energy peaks of 185.2 and 182.8 eV, respectively, which were basically consistent with the previous report of MOF-808 alone.[27] In Fig. 4(d), the C 1s spectrum has three characteristic peaks at 285.1, 286.7, and 289.0 eV, which correspond to the C–C bond, C–O bond, and O–C=O bond, respectively.[28] Fig. 4(c) shows two characteristic peaks of O 1s at 531.9 and 530.2 eV, corresponding to defect/vacancy oxygen (OV) and lattice oxygen (OL), respectively.[29] As shown in Fig. 4(e), the Bi 4f XPS spectrum of pure Bi_2S_3 shows two obvious peaks (164.6 and 159.3 eV), which could be attributed to the $4f_{5/2}$ and $4f_{7/2}$ of Bi^{3+}.[30] In addition, compared with pure Bi_2S_3, Bi 4f

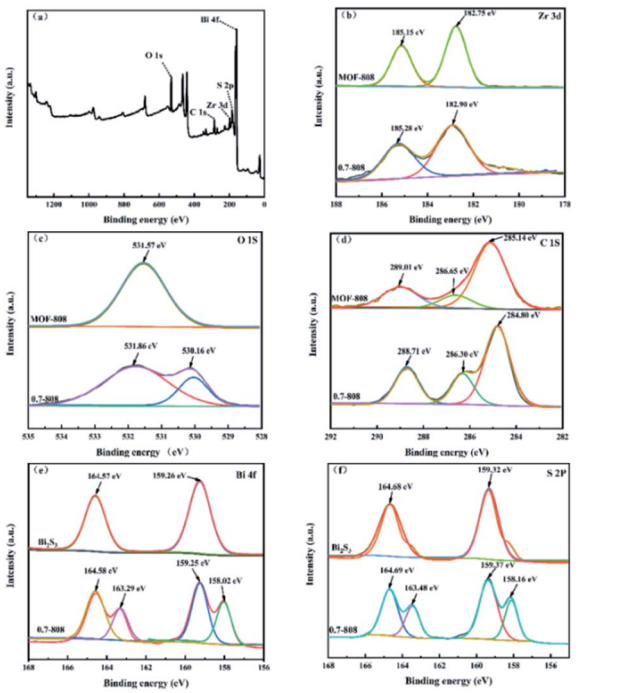

Fig. 4 XPS spectra of the MOF-808, Bi_2S_3 and 0.7-808 (a) survey, (b) Zr 4d, (c) O 1s, (d) C 1s, (e) Bi 4f, and (f) S 2p spectra.

has a split peak at 0.7-808. As shown in Fig. 4(f), the binding energies of the other two characteristic peaks of S 2p were 164.7 and 159.3 eV.[31] In the 0.7-808 complex, S 2p also showed a split peak. It is speculated that there was a relatively strong interaction between the synthesized MOF-808 and Bi_2S_3, which led to the split peak in Bi_2S_3. Based on SEM, XRD, and XPS analyses, it was considered that the compound Bi_2S_3/MOF-808 had been successfully synthesized.

3.1.4 BET analysis. The nitrogen adsorption–desorption curves of MOF-808, Bi_2S_3, and 0.7-808 are shown in Fig. 5. The nitrogen adsorption–desorption curves of simple MOF-808 and the composite material 0.7-808 from Fig. 5(a) belonged to the mixed type I and IV adsorption isotherms. The low-pressure range showed a steep upward trend, indicating that there were a lot of microporous structures; the hysteresis loop in the medium pressure region indicated the existence of a small amount of mesoporous structure. Fig. 5(b) shows the NL-DFT pore-size distribution curve of 0.7-808, and the pore size was less than 5 nm, which again showed that the pore structure of 0.7-808 was dominated by micropores. The specific surface area and pore volume of MOF-808 and Bi_2S_3 and 0.7-808 are shown in Table 1. The BET specific surface area and pore volume of MOF-808 were 545 $m^2\ g^{-1}$ and 0.38 $cm^3\ g^{-1}$, respectively, and the BET specific surface area and pore volume of Bi_2S_3 were 45.3 $m^2\ g^{-1}$ and 0.18 $cm^3\ g^{-1}$, respectively. The BET specific surface area and pore volume of 0.7-808 composite dropped to 410 $m^2\ g^{-1}$ and 0.29 $cm^3\ g^{-1}$. Compared with MOF-808, there were 3–4.5 nm pores in the microporous area. We speculate that a part of the rod-shaped Bi_2S_3 had entered the pores of MOF-808, resulting in changes in its pore structure and internal space, and the other part was partially covering the surface, resulting in a decrease in the specific surface area.

3.1.5 UV-vis analysis. The photocatalytic performance is closely related to the ability to absorb light, so UV-vis diffuse reflectance spectroscopy (UV-vis DRS) was used to test the light-absorption characteristics of the samples, and the results are shown in Fig. 6. Pure Bi_2S_3 had a strong optical absorption capacity in the wavelength range of 200–800 nm. Simple MOF-808 could only absorb ultraviolet light with a wavelength less than 321 nm, while the absorption bands of Bi_2S_3 and MOF-808 composite materials became wider. The light-absorption capacity among all the samples was significantly enhanced, which indicated that the Bi_2S_3 and MOF-808 composites

Table 1 BET surface areas and pore volumes of MOF-808, Bi_2S_3, and 0.7-808 samples

Sample	BET surface area ($m^2\ g^{-1}$)	Pore volume ($cm^3\ g^{-1}$)
0.7-808	410	0.29
Bi_2S_3	45.3	0.177
MOF-808	545	0.383

material had a visible-light response. In addition, the band gap of different catalysts can be calculated by the following equation:

$$\alpha h\nu = A(h\nu - E_g)^{n/2} \quad (1)$$

where α represents the light-absorption coefficient, ν represents the frequency of light, h is Planck's constant, A is the characteristic constant of the material, E_g is the band gap value of the material, and n is an integer, depending on the type of semiconductor optical transition ($n = 1$ is a direct transition; $n = 4$ is an indirect transition).[32] As shown in the figure, the band gap values of Bi_2S_3 and MOF-808 were estimated to be about 1.38 and 4.03 eV, respectively, and these results were consistent with the literature reports.[33]

3.1.6 Electrochemical analysis (impedance, Mott–Schottky). Electrochemical impedance spectroscopy is an effective method to study the charge-transfer dynamics in the interface region.[34] Generally speaking, the smaller the arc in the EIS Nyquist diagram, the smaller the charge-transfer resistance on the electrode surface, and the higher the separation efficiency of photogenerated carriers.[35] Fig. 7 shows the electrochemical impedance spectrum of the composite materials and monomers. Under visible-light conditions, the arc radius of the 0.7-808 composite was the smallest, indicating that the composite had a high electron–hole separation efficiency and fast carrier-transport rate. The photocatalytic degradation efficiency of CP was the highest, which was consistent with the experimental results for the photocatalytic reduction. In addition, the radius of the arc in the EIS Nyquist diagram of MOF-808 was very large, indicating that the separation efficiency of photogenerated electrons and holes of MOF-808 under visible-light irradiation was very low. The composite loaded with bismuth sulfide greatly improved the performance of MOF-808. It can be concluded from the above analysis that the close

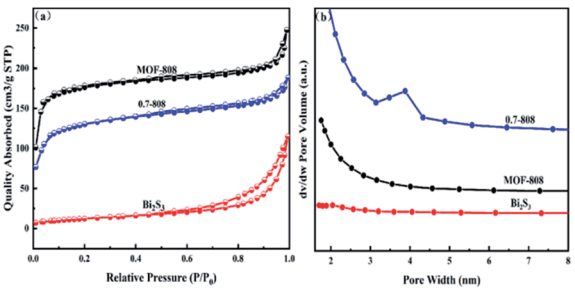

Fig. 5 N_2 adsorption–desorption isotherms (a) and NL-DFT pore-size distributions (b) for MOF-808, Bi_2S_3 and 0.7-808.

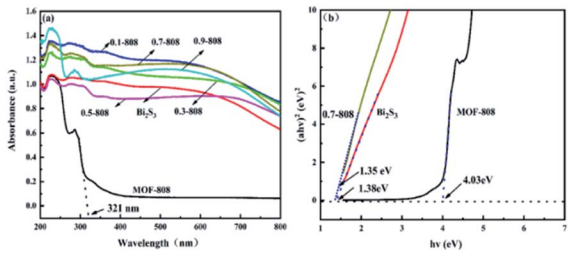

Fig. 6 (a) UV-vis DRS of MOF-808, Bi_2S_3, 0.7-808 and (b) plot of $(\alpha h\nu)^{n/2}$ *versus* $h\nu$.

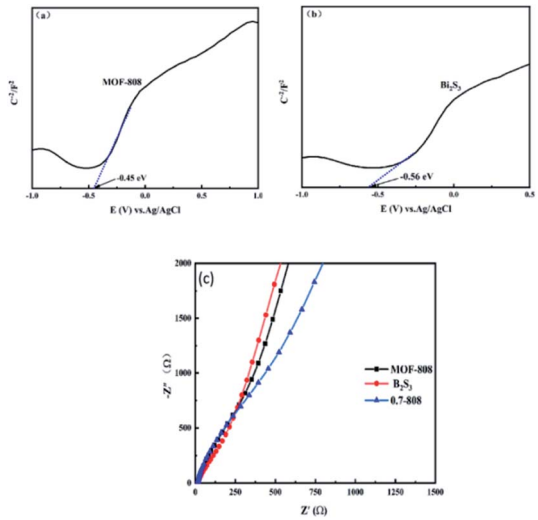

Fig. 7 (a and b) Mott–Schottky plots of MOF-808, and Bi_2S_3; (c) Nyquist plots of EIS for MOF-808, Bi_2S_3 and 0.7-808 composites.

contact between Bi_2S_3/MOF-808 promoted the separation of electron–hole pairs, and further improved the performance of the photocatalyst to degrade tetracycline.

Fig. 7(a and b) present the Mott–Schottky curves of MOF-808 and Bi_2S_3, respectively. The Mott–Schottky curves were measured to determine the band structures of 0.7-808, Bi_2S_3, and MOF-808. It can be seen from the figure that the Mott–Schottky curves of Bi_2S_3 and MOF-808 both had positive slopes, so MOF-808 and Bi_2S_3 were both n-type semiconductors. Among them, the intercept between the linear region of the curve and the X axis is the flat band potential (E_{fb}) of the corresponding semiconductor. From Fig. 7(a and b), the obtained flat band potentials of MOF-808 and Bi_2S_3 were -0.45 and -0.56 V (*vs.* Ag/AgCl), respectively. Generally, the flat band potential is related to the effective electron quantity and carrier concentration, and the bottom of the conduction band of the n-type semiconductor is close to the flat band potential,[36,37] according to the Nernst formula:

$$E_{RHE} = E_{Ag/AgCl} + 0.059\ pH + E^0_{Ag/AgCl} \quad (2)$$

where the value of $E^0_{Ag/AgCl}$ is 0.197 V, and it can be concluded that the conduction band potentials of MOF-808 and Bi_2S_3 relative to the standard hydrogen electrode were -0.253 and -0.363 V, respectively. From the relationship between the conduction band and the valence band:

$$E_{VB} = E_{CB} + E_g \quad (3)$$

From Fig. 6(b), it can be concluded that the band gap width E_g values of MOF-808 and Bi_2S_3 were 4.03 and 1.38 eV, respectively, and the valence band potentials of MOF-808 and Bi_2S_3 were calculated to be 3.78 and 1.02 V, respectively. These characterizations indicated that the interaction between Bi_2S_3 and MOF-808 produced a complex with outstanding photocatalytic degradation properties. The rod-like structure of Bi_2S_3 is conducive to the capture of photoexcited electrons, and MOF-808 provided more catalytic centers, which increased the reaction and adsorption active sites to ensure the photocatalytic degradation ability of 0.7-808.

3.1.7 PL spectra and photocurrent analysis. In order to further understand the reasons for the increased photocatalytic activity of the composite photocatalyst, the PL spectrum was measured to study the separation efficiency of the light-induced charge carriers.[38] Electrons and holes are very important in the photocatalytic reaction process, because the PL spectrum of semiconductors comes from the recombination process of photogenerated electrons and holes, and the lower the intensity of the fluorescence peak, the lower the photogenerated electron–hole recombination rate.[39,40] Fig. 8(a) presents the PL spectra of Bi_2S_3, MOF-808, and the composite material 0.7-808 at an excitation wavelength of 250 nm. It can be seen from Fig. 8(a) that Bi_2S_3, MOF-808 and the composite materials 0.7-808 had a strong emission peak near 393 nm, while the emission peak intensity of 0.7-808 was significantly lower than that of Bi_2S_3 and MOF-808, which indicated that the photoelectric recombination rate of composite 0.7-808 was lower in the process of the photoreaction. This may be because the close contact between the two composite materials and the ligand structure of MOF-808 facilitate the transfer of photogenerated electrons, thereby effectively inhibiting the recombination of electrons and holes. Moreover, it can be concluded from Fig. 8(b) that the photocurrent value of the composite material 0.7-808 was the highest, corresponding also to Fig. 8(a).

3.2 Research on the photocatalytic activity

The photocatalytic performance of the prepared photocatalytic material was evaluated by degradation of an antibiotic contaminant (CP) solution, and the results are shown in the Fig. 9a. When no photocatalyst was added, the pollutants were hardly reduced under visible-light irradiation, indicating that CP had good light stability. Moreover, pure MOF-808 and Bi_2S_3 showed low photocatalytic activity for CP, but the 0.7-MOF-808 composite showed the highest photocatalytic degradation effect, and MOF-808 had a good adsorption capacity for CP solution. For the degradation of antibiotics, as shown in the figure, the simple MOF-808 only had an adsorption effect and could not photodegrade CP, while Bi_2S_3 degraded 45.8% of CP solution. The most active photocatalytic composite material was 0.7-808, where CP was degraded by 80.8% within 60 min. In

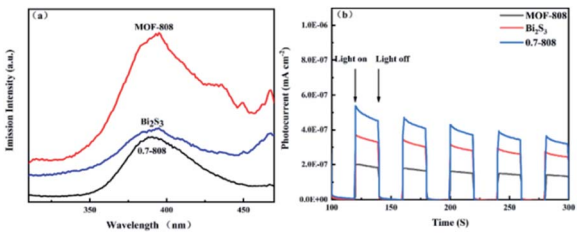

Fig. 8 PL spectra (a) and photocurrent (b) of the MOF-808, Bi_2S_3, and 0.7-808 composites.

order to better study the kinetic characteristics of the photodegradation of CP by materials, the kinetic fitting curve of the degradation of antibiotics was drawn through the experimental data, indicating that the reaction was a first-order reaction, and the reaction equation is:

$$\ln(C/C_0) = Kt \quad (4)$$

where C_0 and C represent the initial concentration of the solution and the concentration at time t, respectively, and K is the rate constant (min^{-1}). The K value of the catalyst obtained by fitting is shown in the illustration. It can be seen from the figure that the K value of MOF-808 alone was 0.0049 min^{-1}, and the K value of Bi_2S_3 was 0.0103 min^{-1}. The 0.7-808 composite material with the best degradation effect had a K value of 0.0290 min^{-1}, which was 5.92 and 2.82 times that of simple MOF-808 and Bi_2S_3, respectively. It can be seen from the figure that the presence of an appropriate amount of MOF-808 caused the agglomeration of Bi_2S_3 nanorods to get the most effective suppression, increases the surface area of the material, and enables it to obtain greater light absorption and to form a tight interface between the two materials. This connection is more conducive to the transfer of photogenerated charges, thereby enhancing the photocatalytic reaction performance.

3.3 Research on the mechanism of photocatalysis

In order to study the catalytic mechanism of the 0.7-808 composite material for the photocatalytic degradation of pollutants, different scavengers, such as isopropanol (IPA), ammonium oxalate (AO), and benzoquinone (BQ), were introduced for when the 0.7-808 composite material degraded CP to capture $^{\cdot}OH$, h^+, and $^{\cdot}O_2^-$,[41] respectively, and the results are shown in Fig. 10(c). In the presence of BQ, the degradation of CP had no significant effect, which indicated that O_2^- was not the main active substance. When AO was added to the reaction, the degradation of CP did not decrease significantly, indicating that h^+ was not the main active species either. However, with the addition of IPA, the degradation of CP was dramatically inhibited, which indicated that $^{\cdot}OH$ played a pivotal role in the degradation reaction of CP, and confirmed that $^{\cdot}OH$ was the main active species in this photocatalytic reaction. With the aim of further exploring the active oxygen of 0.7-808 in the process of photocatalysis, electron spin resonance (ESR) spectroscopy was performed on the sample. DMPO was used as a free radical trapping agent to determine the formation of $^{\cdot}OH^-$ and $^{\cdot}O_2^-$ in the photocatalytic reaction process through the ESR test, and the results are shown in Fig. 10(a and b). No ESR signal was detected in the dark. After turning on the light, the intensity of the characteristic peak of DMPO–$^{\cdot}O_2^-$ was weaker, while the intensity of the characteristic peak of DMPO–$^{\cdot}OH$ was more obvious, which further confirmed that $^{\cdot}OH$ was generated during the photocatalytic reaction. These results all indicate that $^{\cdot}OH$ was the main active species in the photocatalytic degradation.

Based on the above research, we proposed the possible photocatalytic mechanism of 0.7-808 composite photocatalyst

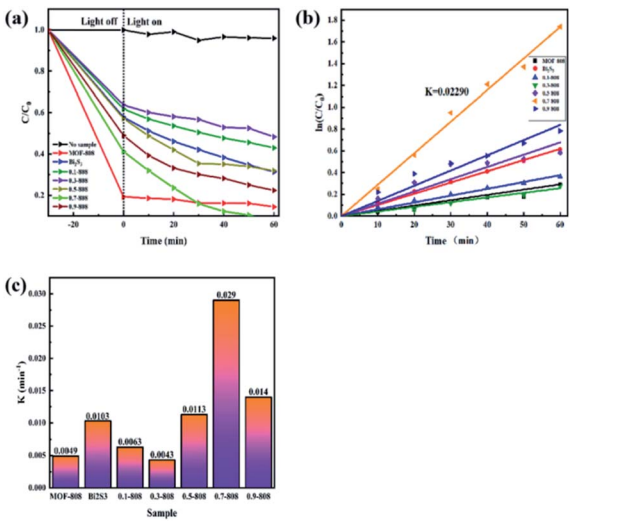

Fig. 9 (a) Influence that the illumination time has on the photocatalytic degradation of the catalysts, (b) the pseudo-first-order dynamics, and (c) the apparent rate constant of the degradation reaction.

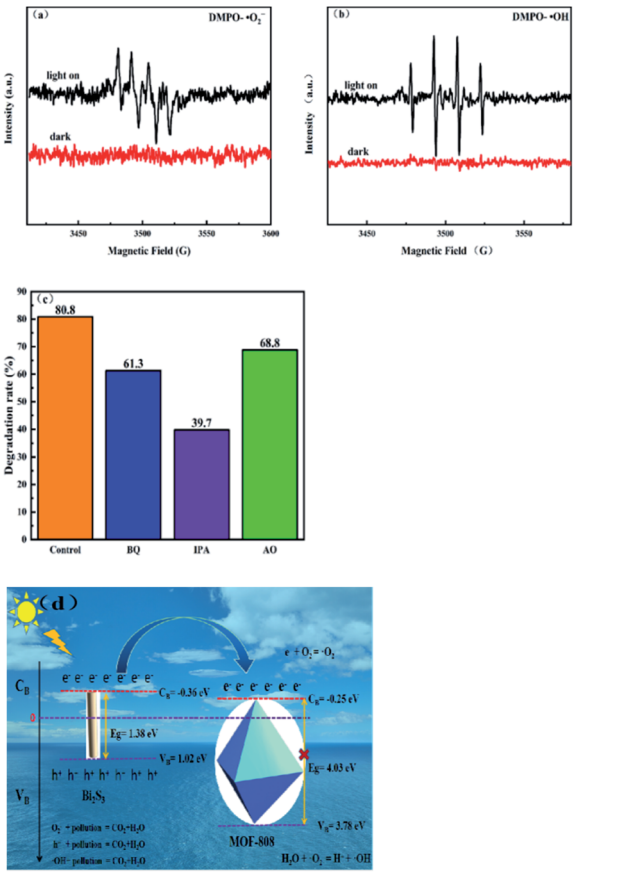

Fig. 10 DMPO spin-trapping ESR spectra for 0.7-808 composites (a) in methanol dispersion for DMPO–$^{\cdot}O_2^-$, (b) in water for DMPO–$^{\cdot}OH$; (c) free radical trapping experiments for the degradation of CP over the 0.7-808 composite; (d) proposed photocatalytic mechanism for the degradation of CP on the surface of the 0.7-808 composite.

to degrade tetracycline. According to literature reports, $^{\cdot}OH^{-}$ is the main influencing substance in Bi_2S_3 photocatalysis.[42] Fig. 10(d) shows the possible photocatalytic mechanism of the 0.7-808 composite photocatalytic material. According to the Mott–Schottky test, the MOF-808 and Bi_2S_3 produced by the reaction were both n-type semiconductors.

When irradiated by visible light, the electrons in the valence band (V_B) of Bi_2S_3 are excited to transition to the conduction band (C_B), leaving more holes in the valence band, forming electron–hole pairs. The conduction band potential of Bi_2S_3 is −0.36 V (*vs.* NHE), which is slightly higher than that of MOF-808 (−0.25 V *vs.* NHE). Therefore, the photogenerated electrons on the conduction band of Bi_2S_3 would migrate to the conduction band of MOF-808. The porous structure of MOF-808 is conducive to the transfer and transmission of electrons. The tetracycline adsorbed on the surface can quickly undergo a reduction reaction with the photogenerated electrons. The conduction band potential of MOF-808 is more negative than the standard redox potential E^0 ($O_2/^{\cdot}O_2^{-}$, −0.046 V *vs.* NHE),[43] so the electrons accumulating on the conduction band of MOF-808 can oxidize the dissolved oxygen in the water and $^{\cdot}O_2^{-}$ is generated; water reacts with the $^{\cdot}O_2^{-}$, and the main active species of this photoreaction is $^{\cdot}OH$. The holes accumulating in the valence band can also directly oxidize with CP molecules. In addition, the bridging ligand of MOF-808 may also speed up the transfer of photoelectrons, thereby improving the photocatalytic activity. Therefore, the close contact of n–n Bi_2S_3/MOF-808 promotes the separation of electrons and holes, and the photocatalytic degradation process of tetracycline. This electron-transfer process can fully inhibit electron–hole recombination, improve the charge-separation efficiency, and further improve the photocatalytic activity.

3.4 Repeatability and stability of the 0.7-808 composites testing

In order to evaluate the possibility of composite catalysts in practical application, reproducibility and stability tests were carried out for the 0.7-808 material. As shown in Fig. 11(a), after the photocatalytic degradation of CP was repeated four times, the fourth repetitive experiment running for 60 min showed a certain decrease in the removal rate of CP, but it was still stronger than the pure monomer. This shows that the 0.7-808 composite photocatalyst has high stability and could be reused in practical application. Therefore, it could be seen that the heterogeneous structure of the composite catalyst not only improved its activity, but also improved its stability. With the aim of further assessing whether the structure of the catalyst was damaged after use, the catalyst was characterized by XRD before and after use, and the results are demonstrated in Fig. 11(b). It can be seen from the figure that the intensity of the XRD diffraction peak of the catalyst was basically unchanged before and after use. Therefore, it could be concluded that the structure of the catalyst was not destroyed after use.

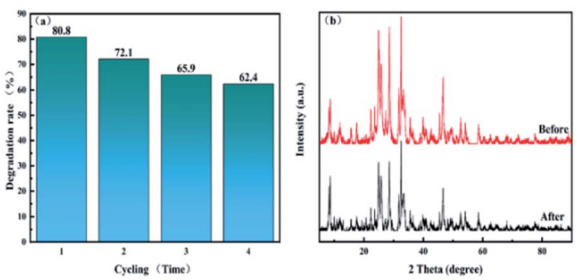

Fig. 11 (a) Cycling runs of 0.7-808 in the degradation of CP under visible light. (b) XRD pattern of 0.7-808 before and after carrying out the photocatalytic experiments.

4. Conclusions

In this paper, a microwave oven was used to prepare porous MOF-808 with a large specific surface area simply and quickly, and then Bi_2S_3/MOF-808 composite materials with different loading ratios were synthesized by a hydrothermal method. Under visible-light irradiation, the photocatalytic reduction performance of the Bi_2S_3/MOF-808 composite material was greatly improved compared with pure Bi_2S_3 and MOF-808, which may be due to the better adsorption performance of MOF-808. The enhanced absorption between MOF-808 and Bi_2S_3 and close contact between MOF-808 and Bi_2S_3 greatly increased the separation rate of photogenerated electron–hole pairs. Therefore, the production of O_2^{-}, $^{\cdot}OH$, and h^{+} was promoted. After 4 cycles, the composite catalyst still had good cycle stability and structural stability.

Conflicts of interest

The authors declare no competing financial interests.

Acknowledgements

We are grateful for grants from Natural Science Foundation of China (No. 21566031).

Notes and references

1 G. Naling, Z. Zhu, D. Hongjun, X. Yao and L. Ziyang, Construction of high-dispersed $Ag/Fe_3O_4/g\text{-}C_3N_4$ photocatalyst by selective photo-deposition and improved photocatalytic activity, *Appl. Catal., B*, 2016, **182**, 115–122.
2 M. Xia, H. Mingjun, Q. Zhang, C. Zhigang and Y. Shengxia, Advanced photocatalytic performance of graphene-like BN modifiied BiOBr flflower-like materials for the removal of pollutants and mechanism insight, *Appl. Catal., B*, 2016, **183**, 254–262.
3 X. Liu, J. C. Steele and X. Z. Meng, Usage, residue, and human health risk of antibiotics in Chinese aquaculture: a review, *Environmental Pollutants*, 2017, **223**, 161–169.
4 J. Han, X. Zheng, L. Zhang, H. Fu and J. Chen, Removal of SO_2 on a nanoporous photoelectrode with simultaneous H_2 production, *Environ. Sci.: Nano*, 2017, **4**(4), 834–842.
5 L. Weitao, W. Jiajun, Z. Jiye, T. Chen and W. Minghong, Simulated solar driven catalytic degradation of psychiatric

drug carbamazepine with binary $BiVO_4$ heterostructures sensitized by graphene quantum dots, *Appl. Catal., B*, 2017, **205**, 587–596.

6 N. Liu, H. Wenyuan, Z. Xiaodong, L. Tang and W. Yuxin, Ultrathin graphene oxide encapsulated in uniform MIL-88A(Fe) for enhanced visible light-driven photodegradation of RhB, *Appl. Catal., B*, 2018, **221**, 119–128.

7 T. Li, C. Jia, Y. Xue, L. Li, A. Wang and G. Xu, Fabrication of compressible and recyclable macroscopic g-C_3N_4/GO aerogel hybrids for visible-light harvesting: A promising strategy for water remediation, *Appl. Catal., B*, 2017, **219**, 241–248.

8 J. Chaoran, L. Ki Yip, M. A. P. Christopher, K. B. Mustafa, L. Chiching, R. Qiushi, J. A. M. Savio, F. L. Adam and T. Junwang, Size-controlled TiO_2 nanoparticles on porous hosts for enhanced photocatalytic hydrogen production, *Appl. Catal., A*, 2015, **521**, 133–139.

9 A. Ning, M. Yuwei, L. Juming, M. Huiyan, Y. Jucai and Z. Qiancheng, Enhanced visible-light photocatalytic oxidation capability of carbon-doped TiO_2 *via* coupling with fly ash, *Chin. J. Catal.*, 2018, **39**, 1890–1900.

10 T. Zhenwei, Y. Dong, X. Tianxiong, T. Yao and J. Zhongyi, Biomimetic fabrication of g-C_3N_4/TiO_2 nanosheets with enhanced photocatalytic activity toward organic pollutant degradation, *Chem. Eng. J.*, 2015, **260**, 117–125.

11 Y. Li, Y. Fang, Z. Cao, N. Li, D. Chen, Q. Xu and J. Lu, Construction of g-C_3N_4/PDI@MOF heterojunctions for the highly efficient visible light-driven degradation of pharmaceutical and phenolic micropollutants, *Appl. Catal., B*, 2019, **250**, 150–162.

12 A. Gómez-Avilés, M. Peñas-Garzón, J. Bedia, D. D. Dionysiou, J. J. Rodríguez and C. Belver, Mixed Ti-Zr metal–organic-frameworks for the photodegradation of acetaminophen under solar irradiation, *Appl. Catal., B*, 2019, **253**, 253–262.

13 D. He, H. Niu, S. He, L. Mao, Y. Cai and Y. Liang, Strengthened Fenton degradation of phenol catalyzed by core/shell Fe–Pd@C nanocomposites derived from mechanochemically synthesized Fe-Metal organic frameworks, *Water Res.*, 2019, **162**, 151–160.

14 C. Wenqian, L. Linyue, L. Li, Q. Wenhui, T. Tang, L. Xu, X. Kejun and W. Mingong, MoS_2/ZIF-8 Hybrid Materials for Environmental Catalysis: Solar-Driven Antibiotic-Degradation Engineering, *Eng*, 2019, **5**(4), 755–767.

15 K. V. Kovtunov, V. V. Zhivonitko, A. Corma and I. V. Koptyug, Parahydrogen induced polarization in heterogeneous hydrogenations catalyzed by an immobilized Au (III) complex, *J. Phys. Chem. Lett.*, 2010, **1**(11), 1705–1708.

16 C. Cheng, F. Jianzhang, L. Shaoyou, C. Chaoping, Y. Chen, L. Ren, F. Weihua and F. Zhanqiang, Zirconium metal–organic framework supported highly-dispersed nanosized $BiVO_4$ for enhanced visible-light photocatalytic applications, *J. Chem. Technol. Biotechnol.*, 2016, **91**(11), 2785–2792.

17 H. Furukawa, F. Gándara, Z. Yuebiao, J. Juncong, W. L. Queen, M. R. Hudson and O. M. Yaghi, Water adsorption in porous metal–organic frameworks and related materials, *J. Am. Chem. Soc.*, 2014, **136**(11), 4369–4381.

18 C. Yumin, J. Qingfeng, L. Huiquan, H. Jingyu, Z. Liangjun, L. Shigang, Y. Zou and J. Yang, Photocatalytic activities of Bi_2S_3/BiOBr nanocomposites synthesized by a facile hydrothermal process, *Appl. Surf. Sci.*, 2014, **290**, 233–239.

19 Z. Zhijie, W. Wenzhong, L. Wang and S. Songmei, Enhancement of Visible-Light Photocatalysis by Coupling with Narrow-Band-Gap Semiconductor: A Case Study on Bi_2S_3/Bi_2WO_6, *ACS Appl. Mater. Interfaces*, 2012, **4**(2), 593–597.

20 Y. Yang, M. Qiangqiang, J. Xiaoliang, M. Sugang, Z. Xiuzhen, Z. Sujuan, F. Xianliang and C. Shifu, Photocatalytic Performance of NiS/CdS Composite with Multistage Structure, *ACS Appl. Energy Mater.*, 2020, **3**(8), 7736–7745.

21 M. Samy, M. G. Ibrahim, M. Fujii, K. E. Diab, M. ElKady and M. G. Alalm, CNTs/MOF-808 painted plates for extended treatment of pharmaceutical and agrochemical wastewaters in a novel photocatalytic reactor, *Chem. Eng. J.*, 2021, **406**, S1385-8947(20)33279-4.

22 C. Ardila-Suárez, D. R. Molina, V. H. Alem, V. G. Baldovino-Medrano and G. E. Ramírez-Caballero, Synthesis of ordered microporous/macroporous MOF-808 through modulator-induced defect-formation, and surfactant self-assembly strategies, *Phys. Chem. Chem. Phys.*, 2020, **22**(22), 12591–12604.

23 S. Lin, Z. Yufeng, J. K. Bediako, C. W. Cho, A. K. Sarkar, C. R. Lim and Y. S. Yun, Structure-controlled recovery of Palladium (II) from acidic aqueous solution using metal–organic frameworks of MOF-802, UiO-66 and MOF-808, *Chem. Eng. J.*, 2019, **362**, 280–286.

24 A. Phuruangrat, T. Thongtem and S. Thongtem, Characterization of Bi_2S_3 nanorods and nano-structured flowers prepared by a hydrothermal method, *Mater. Lett.*, 2009, **63**(17), 1496–1498.

25 T. Thongtem, C. Pilapong, J. Kavinchan, *et al.*, Microwave assisted hydrothermal synthesis of Bi_2S_3 nanorods in flower-shaped bundles, *J. Alloys Compd.*, 2010, **500**(2), 195–199.

26 L. Ullah, Z. Guoying, X. Zichen, H. Hongyan, U. Muhammad and Z. Suojiang, 12-Tungstophosphoric acid niched in Zr-based metal–organic framework: a stable and efficient catalyst for Friedel-Crafts acylation, *Sci. China: Chem.*, 2018, **61**(4), 402–411.

27 G. Wang, C. Sharp, A. M. Plonka, Q. Wang, A. I. Frenkel, W. Guo, C. Hill, C. Smith, J. Kollar, D. Troya and J. R. Morris, Mechanism and Kinetics for Reaction of the Chemical Warfare Agent Simulant, DMMP(g), with Zirconium (IV) MOFs: An Ultrahigh-Vacuum and DFT Study, *J. Phys. Chem. C*, 2017, **121**(21), 11261–11272.

28 Y. Wu, H. J. Luo and H. Wang, Synthesis of iron(iii)-based metal–organic framework/graphene oxide composites with increased photocatalytic performance for dye degradation, *RSC Adv.*, 2014, **4**(76), 40435–40438.

29 M. J. Islam, H. K. Kim, D. A. Reddy, K. Yujin, R. Ma, H. Baek, J. Kim and T. K. Kim, Hierarchical BiOI nanostructures supported on a metal organic framework as efficient photocatalysts for degradation of organic pollutants in water, *Dalton Trans.*, 2017, **46**(18), 6013–6023.

30 H. Zetian He, S. Liu, Y. Zhong, C. Daimei, H. Ding, J. Wang, D. Gaoxiang, G. Yang and Q. Hao, Preparation of $BiPO_4$/graphene photoelectrode and its photoelectrocatalyitic performance, *Chin. J. Catal.*, 2020, **41**(2), 302–311.

31 M. Lu, Y. Guotao, W. Zuoshan, W. Yuyuan and J. Guo, Synthesis of $BiPO_4/Bi_2S_3$ Heterojunction with Enhanced Photocatalytic Activity under Visible-Light Irradiation, *Nanoscale Res. Lett.*, 2015, **10**(1), 385.

32 M. Xiaodong, M. Wanxia, J. Deli, D. Li, M. Suci and M. Chen, Construction of novel $WO_3/SnNb_2O_6$ hybrid nanosheet heterojunctions as efficient Z-scheme photocatalysts for pollutant degradation, *J. Colloid Interface Sci.*, 2017, **15**(506), 93–101.

33 H. Liu, X. Caiyun, L. Dandan Li and J. Hailong, Photocatalytic hydrogen production coupled with selective benzylamine oxidation over MOF composites, *Angew. Chem., Int. Ed.*, 2018, **57**, 1–6.

34 M. A. Mahadadalka, S. W. Gosavi and B. B. Kale, Interstitialcharge transfer pathways in a $TiO_2/CdIn_2S_4$ heterojunction photocatalyst for direct conversion of sunlight into fuel, *J. Mater. Chem. A*, 2018, **33**(6), 16064–16073.

35 M. A. Najeeb, A. Alkareem, M. Awais, Z. Ahmad, R. A. Shakoor, *et al.*, Effect of microwave sintering on the crystal domain and electrical properties of TiO_2 nanoparticles, *J. Nanopart. Res.*, 2017, **19**(6), 199–208.

36 Z. Dai, F. Qin, Z. Huiping, F. Tian, L. Yunling and C. Rong Chen, Time-dependent evolution of the $Bi_{3.64}Mo_{0.36}O_{6.55}/Bi_2MoO_6$ heterostructure for enhanced photocatalytic activity *via* the interfacial hole migration, *Nanoscale*, 2015, **28**(7), 11991–11999.

37 J. Yan, T. Wang, G. Wu, W. Dai, N. Guan, L. Li and J. Gong, Nanosheets: tungsten oxide single crystal nanosheets for enhanced multichannel solar light harvesting, *Adv. Mater.*, 2015, **27**, 1580–1586.

38 Y. Huang, W. Fan, B. Long, H. Li, F. Zhao, Z. Liu, Y. Tong and H. Ji, Visible light $Bi_2S_3/Bi_2O_3/Bi_2O_2CO_3$ photocatalyst for effective degradation of organic pollutions, *Appl. Catal., B*, 2016, **185**, 68–76.

39 A. Gómez-Avilés, M. Peñas-Garzón, J. Bedia, D. D. Dionysiou, J. J. Rodríguez and C. Belver, Mixed Ti-Zr metal–organic-frameworks for the photodegradation of acetaminophen under solar irradiation, *Appl. Catal., B*, 2019, **253**, 253–262.

40 D. He, H. Niu, S. He, L. Mao, Y. Cai and Y. Liang, Strengthened Fenton degradation of phenol catalyzed by core/shell Fe–Pd@C nanocomposites derived from mechanochemically synthesized Fe-Metal organic frameworks, *Water Res.*, 2019, **162**, 151–160.

41 X. M. Lv, J. X. Wang, Z. X. Yan, *et al.*, Design of 3D h-BN architecture as Ag_3VO_4 enhanced photocatalysis stabilizer and promoter, *J. Mol. Catal. A: Chem.*, 2016, **418–419**, 146–153.

42 T. Zhao, X. F. Zhu, Y. F. Huang and Z. J. Wang, One-step hydrothermal synthesis of a ternary heterojunction g-C_3N_4/Bi_2S_3/In_2S_3 photocatalyst and its enhanced photocatalytic performance, *RSC Adv.*, 2021, **11**(17), 9788–9796.

43 S. Leqiang, J. Deli, P. Xiao, Z. Liming, M. Suci and M. Chen, Enhancement of g-C3N4 nanosheets photocatalysis by synergistic interaction of ZnS microsphere and RGO inducing multistep charge transfer, *Appl. Catal., B*, 2016, **198**, 200–210.